

Lawrence Berkeley National Laboratory

Lawrence Berkeley National Laboratory

Title

Nanoscale Pore Imaging and Pore Scale Fluid Flow Modeling in Chalk

Permalink

<https://escholarship.org/uc/item/9b86t01t>

Authors

Tomutsa, Liviu
Silin, Dmitriy

Publication Date

2004-08-19

NANOSCALE PORE IMAGING AND PORE SCALE FLUID FLOW MODELING IN CHALK

LIVIU TOMUTSA, DMITRIY SILIN

Earth Sciences Division, Lawrence Berkeley National Laboratory, Berkeley, CA, U.S.A.

ABSTRACT

For many rocks of high economic interest such as chalk, diatomite, tight gas sands or coal, nanometer scale resolution is needed to resolve the 3D-pore structure, which controls the flow and trapping of fluids in the rocks. Such resolutions cannot be achieved with existing tomographic technologies. A new 3D imaging method, based on serial sectioning and using the Focused Ion Beam (FIB) technology has been developed. FIB allows for the milling of layers as thin as 10 nanometers by using accelerated Ga⁺ ions to sputter atoms from the sample surface. After each milling step, as a new surface is exposed, a 2D image of this surface is generated. Next, the 2D images are stacked to reconstruct the 3D pore or grain structure. Resolutions as high as 10 nm are achievable using such a technique. A new robust method of pore-scale fluid flow modeling has been developed and applied to sandstone and chalk samples. The method uses direct morphological analysis of the pore space to characterize the petrophysical properties of diverse formations. Not only petrophysical properties (porosity, permeability, relative permeability and capillary pressures) can be computed but also flow processes, such as those encountered in various IOR approaches, can be simulated. Petrophysical properties computed with the new method using the new FIB data will be presented. Present study is a part of the development of an Electronic Core Laboratory at LBNL/UCB.

INTRODUCTION

To model multiphase flow in porous media at pore scale, 3D volume data are needed with a resolution adequate for the pore system studied. In the last decade, X-ray microtomography has been used extensively for direct visualization of pore system and the fluids within sandstone (Jasty, J.K. *et al*, 1993, Coles *et al*, 1996, Wildenschild *et al*, 2002, Seright *et al*, 2003). While this approach is relatively fast and nondestructive, its applicability is mostly limited to micron resolutions, although recent developments are bringing the resolution to submicron range (Stampanoni *et al*, 2002). For chalk pore systems, which have submicron to nanometer scale characteristic length scales, 3D stochastic methods based on 2D scanning electron microscope (SEM) images of thin sections have been used to reconstruct the pore system (Talkudar *et al*, 2001). The advent of the Focused Ion Beam technology has made it possible to reconstruct directly the 3D submicron chalk and diatomite pore structures from successive 2D images (Tomutsa and Radmilovic, 2003). The advantage of the FIB technology is that it can be used to directly image 3D volumes in selected regions in relatively large samples. FIB technology has been used extensively in microelectronics to access individual components with nanoscale accuracy for design verification, failure analysis and circuit modification (Orloff *et al*, 2002). It also has been used in material sciences for sectional sample preparation for SEM and for 3D imaging of alloys components (Kubis *et al*, 2004). In earth sciences, FIB has been used for sample preparation for SEM and to access inner regions for performing microanalysis (Heaney *et al*, 2001). To directly access the pore structure at submicron scale, FIB is used to mill successive layers of the rock material as thin as 10 nm. As successive 2D surfaces are exposed, they are imaged using either the electron or the ion beam and, after processing, the images are stacked to reconstruct the 3D pore structure. To analyze the 3D chalk images obtained by the FIB method, we applied a recently developed technique (Silin *et al*, 2003). A distinctive feature of this approach is that the 3D pore space image is analyzed directly, bypassing construction of pore networks. Depositional models offer an opportunity to clone such images at practically arbitrary resolutions (Øren and Bakke, 2002; Jin *et al*, 2003). However, extraction of a simple but representative network of pore throats linking pore bodies still remains a nontrivial task (Lindquist, 2002). Moreover, the granular structure of carbonates is tremendously more complex than of “classical” sedimentary rocks like, for example, sandstones, and the pore network extraction methods based on relatively simple grain shapes (Øren and Bakke, 2002) may be not always feasible. Although pore-

network based flow modeling approach enjoyed a significant interest from the researchers and resulted in theoretically and practically sound conclusions (Øren *et al.*, 1998; Patzek, 2001; Blunt, 2001), we feel that direct pore space analysis deserves more attention. In addition, direct analysis of the pore space provides an opportunity to study alteration of the rock flow properties due to mechanical transformations (Jin *et al.*, 2004).

EXPERIMENTAL

Equipment

The FIB apparatus used in this study is model FEI Strata DB235, dual electron and ion beam. It is a scanning electron microscope (SEM) that has also the capability to focus gallium ions (Ga⁺) accelerated by potentials up to 30kV (Fig. 1). Both, secondary electrons and secondary ions can be used for imaging and the digitized images are stored in 1024×954, 8 bit, TIF format. The image contrast is determined both by the topography of the sample and by the difference in the atomic numbers of the materials present at the sample surface. Thus, the required pore/grain contrast can be achieved for epoxy-impregnated as well as nonimpregnated samples. To avoid damaging the sample by the ion beam during imaging, a low beam current (10-100 pA) and a short imaging time (seconds) are recommended. During milling, the ion beam current can be increased by orders of magnitude (up to 20,000 pA) and the exposure time can be increased up to hours. An important feature of the instrument is a 5-axis computer-controlled stage, which allows for repeatable access to the same location on the sample surface. The stage allows for the sample orientation either normal to the ion beam for drilling submicron scale patterns, or quasi parallel for milling successive layers. The large sample chamber and the number of ports present allows for installation of various other instruments (element analysis, platinum deposition, *etc.*) (Fig. 2).

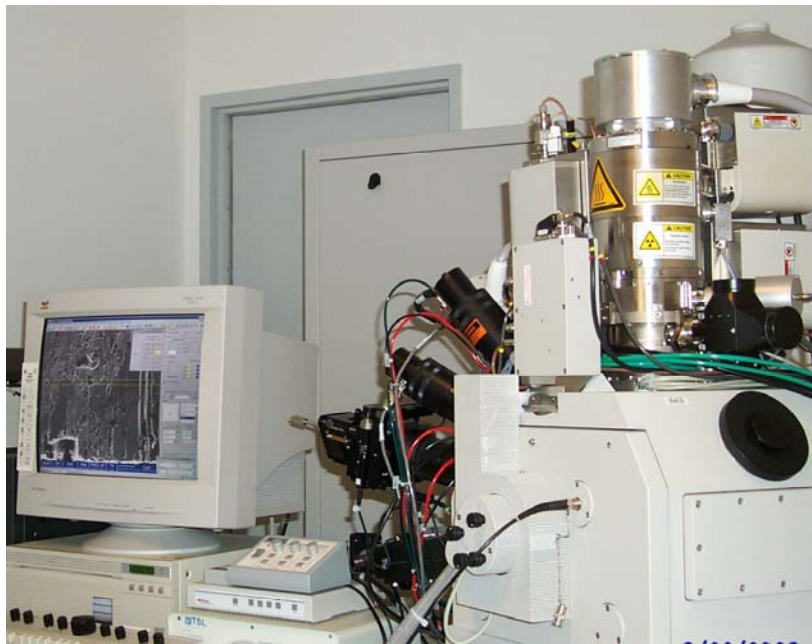


Figure 1. FIB apparatus with both ion and electron columns

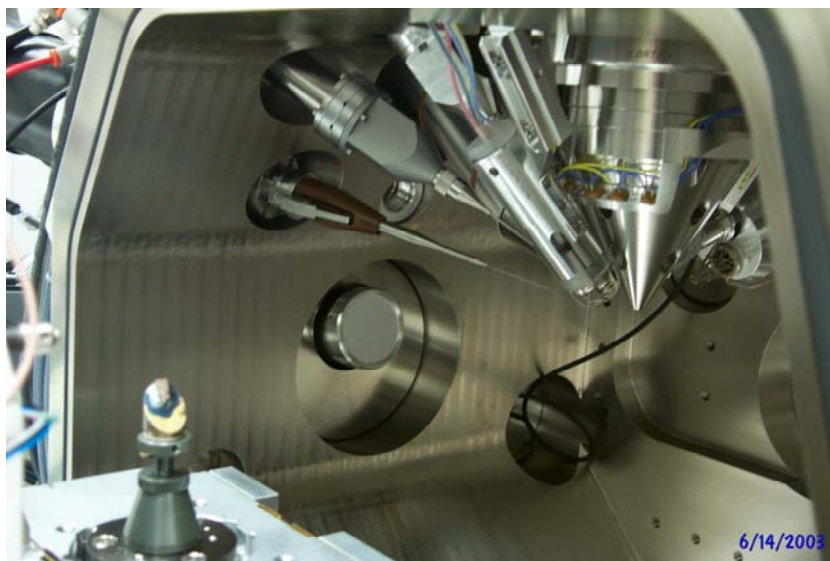


Figure 2. FIB Sample chamber with sample mounted on 45 deg stage

Methodology

To perform 3D imaging using FIB technology, the samples are prepared using standard SEM procedures, *i.e.* cleaning, cutting, polishing, mounting and carbon coating. Good sample cleaning is important to minimize hydrocarbon contamination of the instrument and interference with the high vacuum. Because the FIB mills submicron layers, the initial sample surface has to be flat at the micron scale. High roughness of the sample surface can significantly increase the time required for the FIB to mill the surface to the flatness required for serial sectioning. For soft materials, such as diatomite, a microtome can be used while for harder materials or epoxy impregnated samples, diamond saw cutting and standard thin section procedures for polishing is recommended. The prepared sample is mounted on a 45 degrees SEM stub using conducting adhesive (Fig. 3). As seen in Figure 3, ion milling and SEM imaging can be performed without moving the sample, except for minor refocusing. The SEM approach is the preferred mode of operation from the point of view of increased productivity and improved registration of images if there is a good contrast between the pore space and the matrix, and the charge build up on the sample is not too rapid. The ion beam imaging yields better quality images than the electron beam imaging, due to less charging of the surface, but it is significantly more time consuming to implement due to sample repositioning and refocusing between the milling and imaging steps. Once the volume to be imaged has been defined (Fig. 4), for a constant ion beam current, the depth milled is proportional with the time elapsed. Thus, images captured at equal time intervals present equidistant surfaces at increasing depths within the sample volume. The time required to mill a certain quantity of material depends on the ion current and the sample material.

For example, the time required to mill a volume $50 \times 50 \times 0.1 \mu\text{m}$ in chalk is of the order of minutes, for 30 kV, 3000 pA Ga⁺ ions beam. Higher currents (7000-20,000 pA) will cut faster, but also will yield rougher surfaces, and negatively affect the image quality. Very clean flat surfaces, in which the pore-grain boundaries appear in high contrast, can be generated with no apparent distortion of the pore boundaries. The pore/matrix contrast is more pronounced in an epoxy-impregnated sample than in samples not impregnated. After each milling episode, images are acquired at a selected magnification such that each view captures the desired number of pores with the adequate resolution. Next, the individual 2D images are stacked and aligned using registration (fiducial) markings or characteristic features within the sample volume. Before stacking the 2D images into 3D data sets, the images are segmented. The segmentation of the data into pore/nonpore voxels can be performed either on the 2D images or on the 3D data sets. For images with high pore/nonpore gray scale contrast, simple thresholding could be adequate (Fig. 5). For lower-contrast images, which can benefit from using spatial information besides gray level, other methods, such as indicator krigging are available (Oh and

Lindquist, 1999) or (Mardia-Hainsworth, 1988). A review of various segmentation approaches has been presented by Lindquist (2002). To process the data, a standard image processing software package like Adobe Photoshop can be used for image alignment and contrast equalizing. Image-J from National Institute of Health (rsb.info.nih.gov/ij/) and 3DMA from State University of New York (www.ams.sunysb.edu/~lindquis/3dma/3dma`rock.html#Sec_seg) can be used for batch image manipulation and segmentation.

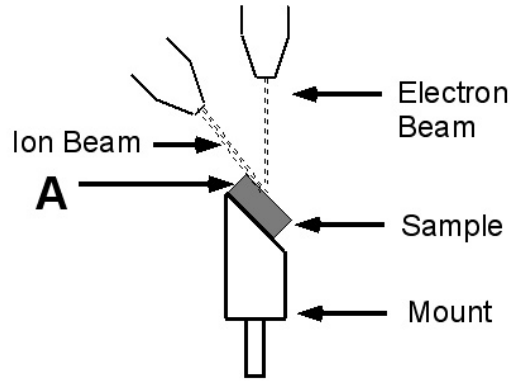


Figure 3. Sample mounted for FIB milling and imaging.



Figure 4. View from the ion beam direction of sample surface A during milling. The milling boundary is defined by the yellow rectangle and the most recent surface exposed is marked by the red segment

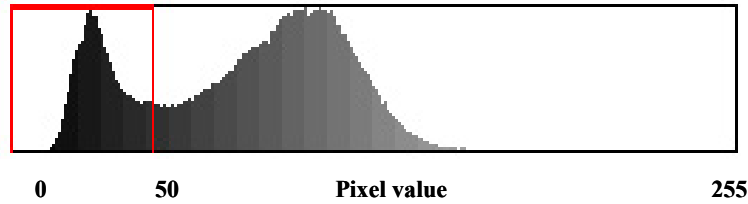


Figure 5. Histogram displaying a high pore/grain contrast. Pore pixel values in 0-50 interval.

Experimental Results

The sample studied, courtesy of ConocoPhillips, was a 1 in diameter Ekofisk plug with 29% He porosity and permeability of 4 md. The sample was CT scanned (1mm thick slices, 133 kV, 120 mA) and a porosity distribution was determined. As seen in the four representative crosssections shown in Figure 6, the sample has a uniform porosity, except for a few mm-scale low porosity regions apparent both on CT and visually. The mean CT measured porosity is 29% and in the low porosity regions is 25%. The 6×4×2 mm sample selected for imaging was from a region with 29% porosity. The sample was epoxy impregnated under vacuum, followed by up to 1400 psi pressure. It was polished following standard thin section preparation techniques using up to 1 μm size diamond polishing disk. The chalk sample presented a good contrast between the epoxy-filled pore space and the matrix, which allowed for secondary electron imaging (SED detector) at 5 kV electron energy by using a 12 s scan, with minimal charging taking place (Fig. 7). The pixel resolution was 0.05 μm. The sections imaged were spaced 0.1 μm apart. To create 0.05 μm cubic voxels, the number of 2D images was doubled by using interpolation between consecutive layers by a spline-based algorithm TransformJ (Meijering, 2001). The good contrast allowed for direct thresholding of the layers to generate a 3D binary image using ImageJ package. A 3D reconstruction of a subset of the binary data is shown in Figure 8.

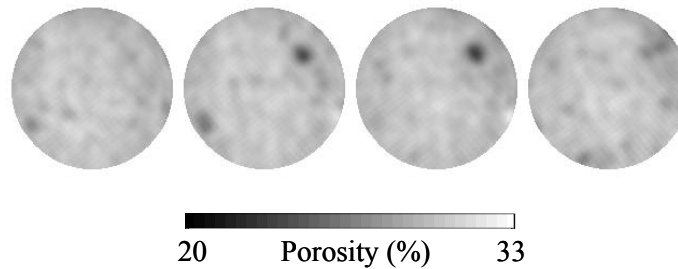


Figure 6. CT derived porosity crosssections of chalk plug

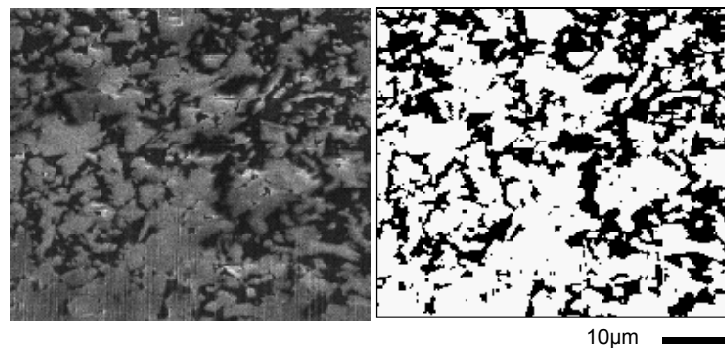


Figure 7. SEM image of FIB prepared surface, before (left) and after segmentation (right)

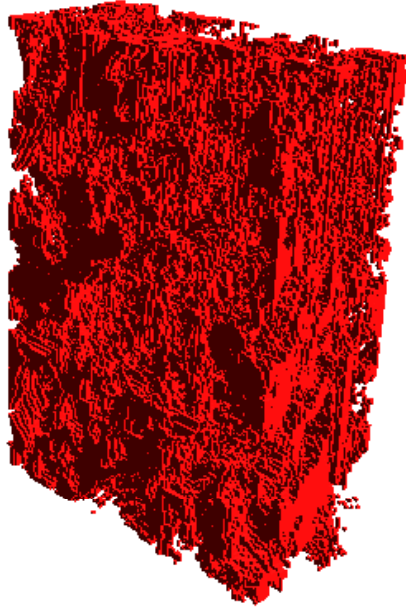


Figure 8. 3D pore reconstruction of $22 \times 32 \times 10 \mu\text{m}^3$ (200×450×636 voxels) chalk volume

PORE SPACE ANALYSIS

The method used in this study is based on the concept of a maximal ball. A similar approach was applied previously to analyze statistically reconstructed media (Magnani *et al.*, 2000). The principle idea is to compute the part of the pore space occupied by wetting and non-wetting fluid, respectively. At a given capillary pressure, one can evaluate the curvature of the fluid-fluid interface. Such an interface, in turn, can be approximated by a spherical surface of the corresponding radius. Therefore, the part of the pore space occupied by the non-wetting fluid can be represented as the union of all balls of this radius, which can be inscribed into the pore space. An extended set of rules can be applied to model a mixed wettability environment and/or nonzero contact angle. This procedure presents an approximate picture of the fluid distribution. There are several sources of possible inaccuracies. The fluid-fluid interface may be not always perfectly spherical. In addition, the curvature of the union of spheres of a given radius, in general, is different from the curvatures of individual spheres. However, all such effects are expected to be concentrated near the pore walls, where such an approximate interface description should not introduce large volumetric errors.

To eliminate artifacts of imaging errors, before any further computations, the data set is first “cleaned” by removing small isolated clusters of solid phase inside pores and small isolated pores inside the solid phase. Cluster search algorithms (Silin and Patzek, 2003) were used. To determine, whether the cluster of voxels is isolated or not, different connectivity rules can be applied: 6-connectivity, where two voxels are connected if they have a common face, 18-connectivity, where two voxels are connected if they have a common edge, and 26-connectivity, where a common vertex between two voxels implies connection. In the elimination of the isolated pores and “solid dust”, the 6-connectivity was applied. This strict rule turned out to be most efficient for a cleanup operation because otherwise artifacts like narrow branches of voxels protruding into the pores significantly perturbed occupation and invasion rules in the percolation simulations.

After the preliminary cleaning, the following two major steps were performed as part of the numeric procedure. First, for each voxel, the squared radius of the largest ball centered at this voxels was computed. Use of squared radii makes it possible to operate with integer variables only, and eliminates all round-off errors. Second, each

voxel of the pore space was assigned a value equal to the maximal squared radius of the ball included in the pore space and including this voxel. Once such a three-dimensional table is setup, various types of analysis can be performed using scanning algorithms and by grouping voxels into clusters with specific properties. In invasion percolation simulations, 18-connectivity rule was applied. The nonwetting fluid connectivity also was verified using the 18-connectivity rule. This rule was selected because it yields clusters of voxels most appropriate for fluid flow simulations using the lattice-Boltzmann or other methods.

Assigning to each voxel the maximal squared radius of a ball, which is inside the pore space and which covers this voxel, is an auxiliary procedure from the point of view of the main objectives of the study. However, it produces some information about the pore space structure. To see how this information can be used, let us consider a simple two-dimensional illustrative example. An ellipsoid is discretized and segmented into a set of pixels, Figure 9. For each pixel, the squared radius of the maximal discrete circle inscribed in the pore space and centered at this pixel is evaluated. The result is displayed on the left-hand picture. However, after assigning to each pixel the squared radius of the maximal covering disk, the picture is different, Figure 9 on the right. Almost all pixels in the ellipsoidal “pore” have the same number. The centers of the two maximal disks with maximal radii are highlighted. Thus, if the number of voxels with a large radius-squared assigned is large, it is an indication of the presence of a pore body or pores of respective size, which are surrounded by smaller openings.

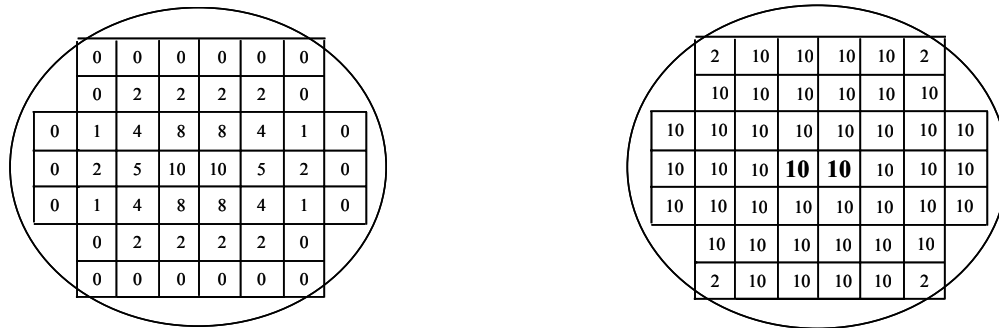


Figure 9. Digitized ellipsoid. The left-hand picture displays maximal squared radii of the circles contained in the pore space and centered at each voxel. The right-hand picture displays maximal squared radii of the covering disks. The highlighted voxels are the centers of those disks.

Figure 10 presents the bar plot of squared radii distribution in the 200×636×450 voxels image of chalk and, for the purpose of comparison, a similar distribution for a 400×400×400 CT image of Fontainebleau sandstone (courtesy of Schlumberger). Note that the resolution for the chalk data is two orders of magnitude higher than that for the sandstone. The bars corresponding to the smallest radii have been removed from the chalk diagram in order to present both plots in comparable scales. Large number of single-voxel “corners” in the chalk could be due to slight misalignment of individual 2D images: microscopic misalignments of the layers may create numerous small corners. The “spectral decomposition” of the pore space in Figure 10 suggests that the presence of few relatively large pores is a distinguishing feature of chalk. The radii distribution of sandstone is more uniform. This fact has a noticeable impact on the shape of capillary pressure curve, as described below.

The squared radii table was used to simulate equilibrium fluid distribution in the pore space at different capillary pressures. The dimensionless capillary pressure curve provides information about the pore space geometry and characteristic dimensions of the pores. Different types of rock are, in particular, characterized by different curves. Dimensionless capillary pressure curves were plotted at different resolutions and for different fragments of the same image in order to investigate the heterogeneity of the sample and the impact of the image resolution on the output.

To test the sample for heterogeneity, the $200 \times 450 \times 636$ data set was split into cubic parts of dimensions $200 \times 200 \times 200$. Some parts overlap each other. For each fragment, the squared radii distribution and the dimensionless capillary pressure curve were calculated. The left plot in Figure 11 shows all the radii squared distributions plotted in the same coordinate axes. A comparison of this plot to a similar plot for the entire image, Figure 10, suggests that the general structure of larger pores is preserved. However, since some pores can be cut into parts by partitioning the the entire image, the distribution can be distorted. The openings near the boundary of the image are analyzed using the convention that the pore space structure is mirrored over the boundary plane.

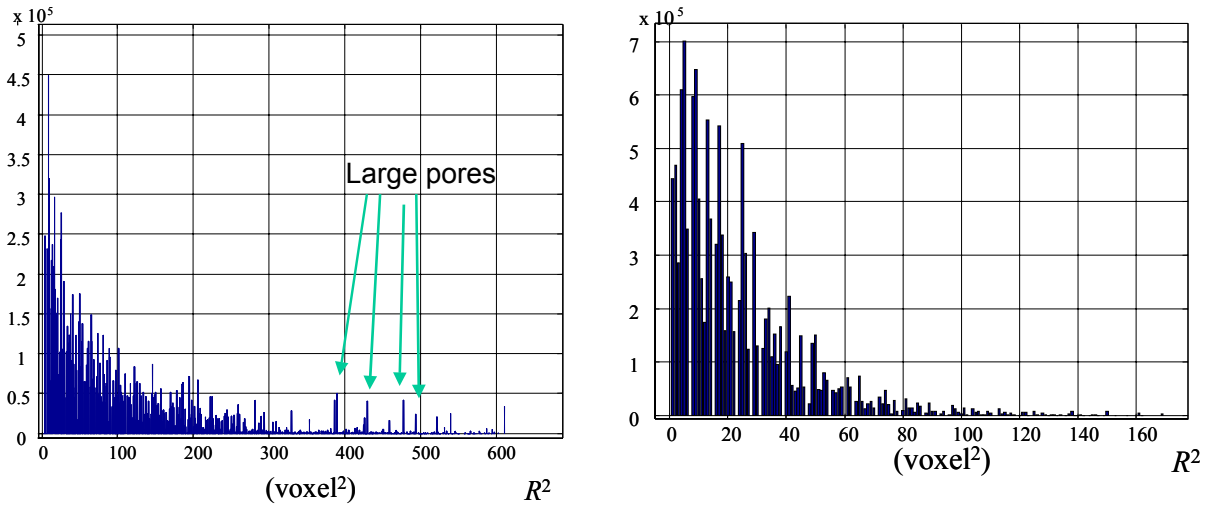


Figure 10. “Spectral analysis” of the pore space. Maximal radii distribution indicating presence of several large pores in the images of chalk plug (left-hand picture) and more uniform distribution of the pore sizes of Fontainebleau sandstone (right-hand side picture). Note that the resolution of the chalk image is $0.05 \mu\text{m}$ and for sandstone is $5 \mu\text{m}/\text{voxel}$.

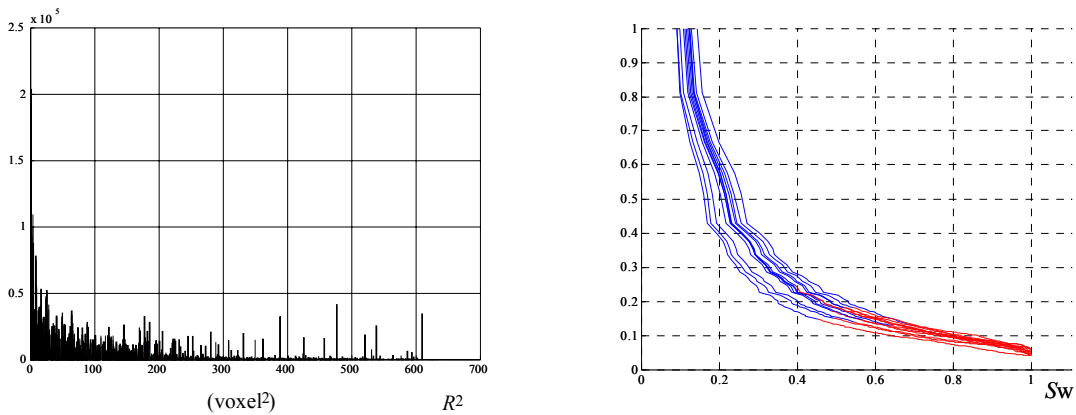


Figure 11. Squared radii distribution and dimensionless capillary pressure curves for twelve different $200 \times 200 \times 200$ voxel fragments. The difference between the curves indicates heterogeneity of the sample.

Comparison among dimensionless capillary pressure curves corresponding to the different parts of the image (the right-hand side plot in Figure 11) suggests that there is significant heterogeneity. Indication of such heterogeneity is noticeable in the radii distribution plot, Figure 11, as well. Due to the presence of several relatively large pores, the fragments, which include those pores, must have a larger porosity and show lower capillary pressures. Apparently, the two separate curves in the right-hand side plot in Figure 11, lying below

the other curves, correspond to such fragments. The red part of each curve corresponds to the saturations, at which the nonwetting fluid is disconnected. Again, one can see that the curves, which are apparently associated with larger openings, show connectivity at higher saturations. Note that such local microscopic heterogeneity in Fontainebleau sandstone (in the respective length scale) is much lower, (Silin *et al.*, 2003).

The dimensionless capillary pressure curves calculated based on simple percolation do not account for the history of fluid migration. Implicitly, it is assumed that the pore space is initially saturated with a nonwetting fluid. Therefore, the curves obtained by modeling simple percolation better reflect the imbibition capillary pressures rather than those of primary drainage. Once the nonwetting fluid becomes disconnected and is trapped, its flow practically stops. Therefore, only the blue portions of the presented curves are physically measurable. The loss of connectivity at 50-70% saturation is in good agreement with experimental results reported for a Ekofisk sample with similar petrophysical properties (Spinler and Baldwin, 1997, Figures 14 and 17). In present work, the simulations account for positive capillary pressures only, which correspond to spontaneous equilibrium fluid distribution. Since spontaneous imbibition is intrinsically a non-equilibrium process, dynamic simulations of such a process require certain modifications of the steady-state capillary pressure curves (Barenblatt *et al.*, 2003; Silin and Partzek, 2004).

At any given radius squared, that is, at any given capillary pressure, the algorithm finds all clusters occupied by the wetting and nonwetting fluid, analyzes the connectedness of the clusters, and seeks clusters spanning between inlet and outlet faces. The fluid distribution can be visualized in order to observe how the fluids “displace” one another. In addition, sequences of such images provide information about the 3D structure of the pore space, which is practically impossible to obtain just by analyzing two-dimensional cross-sections. In Figure 12, the fluid configurations are displayed at several saturations in a fragment of dimensions 100×100×100 voxels. It is noticeable that the nonwetting fluid gets disconnected at a low wetting fluid saturation, which is lower than the typical 50-70% saturation obtained for larger images. This can be related to the fact that some flow paths have a very complex geometry and pass across several adjacent parts.

To scale the capillary curves, computations on a sample with dimensions 10×22.5×32.8 μm and its middle part 5×22.5×32.8 μm were performed. The difference in the size of the image in different directions is implied by the FIB imaging method. For each direction, it was assumed that the sample is open only in this direction and sealed at all other faces. Also, additional simulations were performed under the assumption that all the faces of the sample were open for the flow. Invasion percolation simulations were carried out using cluster search algorithms (Silin and Patzek, 2003). The image of the same core sample was taken at three different resolutions: 0.05 μm , 0.1 μm and 0.2 μm . It was assumed that the surface tension coefficient between the fluids is equal to 20 dynes/cm that is a reasonable value for water-oil interface (Muskat, 1949). The scaled capillary pressure curves are gathered in Figures 13 and 14. The plots show that for large wetting fluid saturations and low capillary pressures the results are consistent for all three resolutions. However, at lower saturations and, respectively, higher capillary pressures, the 0.2 μm resolution is insufficient. The shapes of invasion-percolation curves and the absolute values of capillary pressures are in agreement with the drainage capillary pressure curve reported in Spinler and Baldwin, 1997. The presence of relatively large pores results in almost horizontal segments of invasion-percolation capillary pressure curves. Indeed, to pass a “bottleneck” leading into a larger opening, the capillary pressure needs to reach a certain threshold value, the entry capillary pressure. Once this pressure has been reached, the nonwetting fluid fills the large pore and the nonwetting fluid saturation increases abruptly. The shape and the capillary pressure values computed from simple percolation curves resemble those of the imbibition curve, Figure 15. In all cases, the computed and experimental curves are more similar at saturations, for which the nonwetting fluid is still connected.

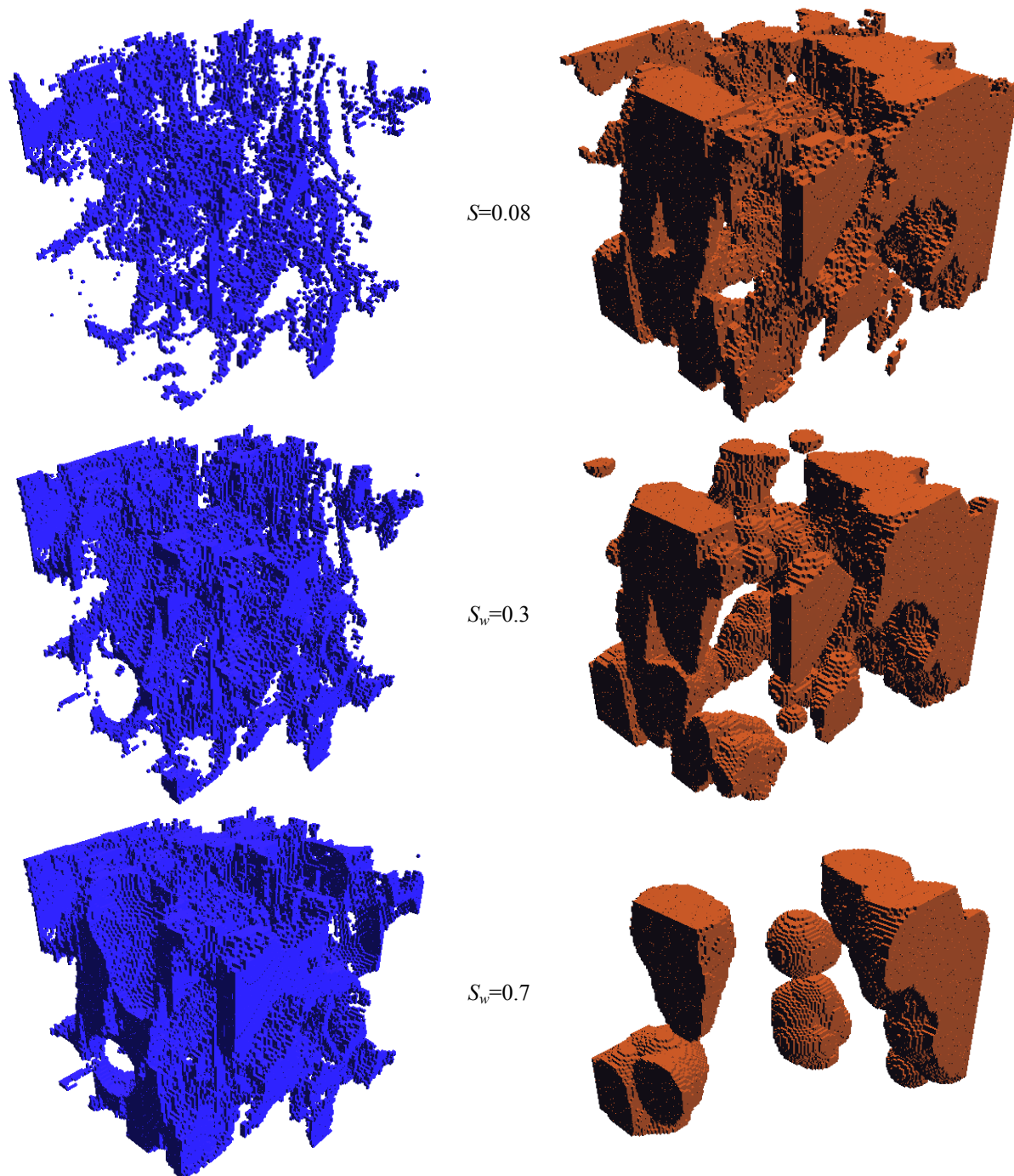


Figure 12. Fluid distributions at different saturations in a $100 \times 100 \times 100$ voxels fragment. The wetting fluid (left-hand column) has the tendency of occupying the corners and roughness, whereas the nonwetting fluid (right-hand column) is in the central parts of the pores. At $S_w=0.3$, one observes that the nonwetting fluid is almost disconnected and at $S_w=0.7$ the nonwetting fluid separates into disconnected droplets..

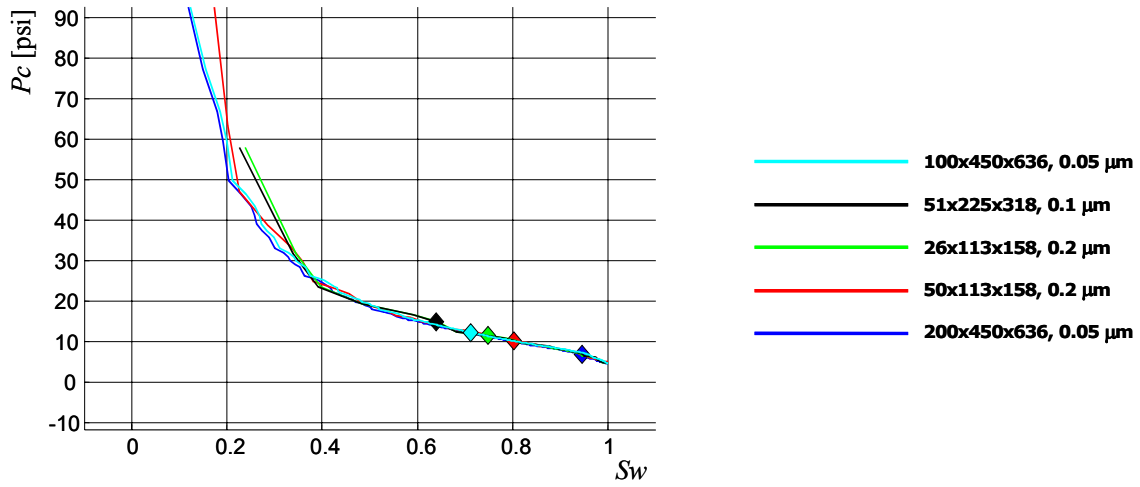


Figure 13. Scaled ordinary-percolation capillary pressure curves computed at different resolutions. The diamonds denote the points where the nonwetting fluid becomes disconnected.

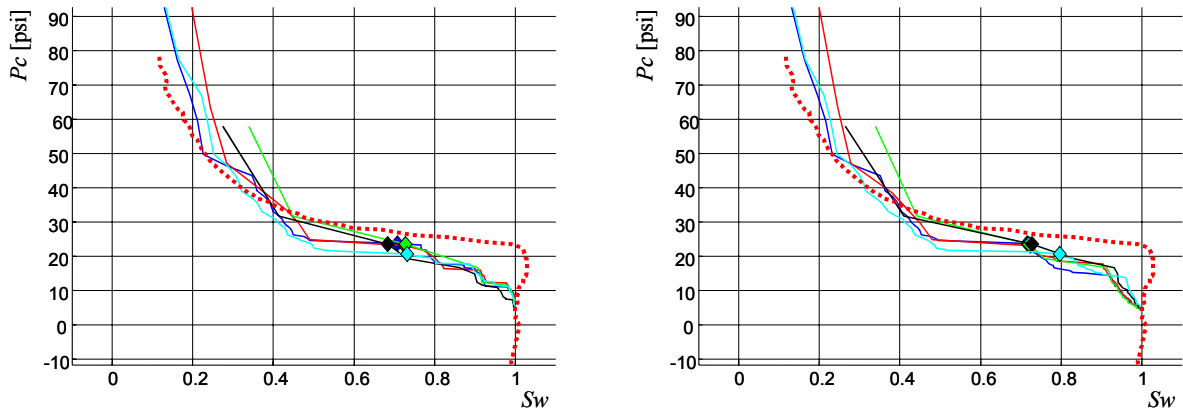


Figure 14. Comparison of scaled invasion-percolation capillary pressure curves in two different directions (solid lines) with experimental drainage capillary pressure curve digitized from Spinler and Baldwin, 1997 (red dotted lines). The diamonds denote the points where the nonwetting fluid becomes disconnected. Different colors denote different resolutions in the same way as in Fig. 13.

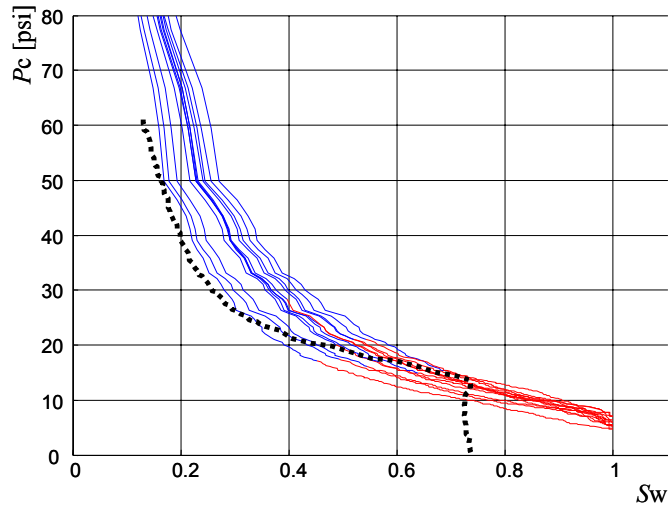


Figure 15. Scaled dimensionless capillary pressure curves (Fig. 11) (solid lines) are plotted together with experimental capillary pressure imbibition curve (black dotted line) digitized from SCA-9705 (Fig. 14).

SUMMARY AND CONCLUSIONS

A new method of sample serial sectioning and imaging using FIB technology has been used to image with submicron resolution the 3D pore structure of chalk. FIB was used to mill successive sample layers as wide as 50 μm and as thin as 0.1 μm by sputtering of atoms from the sample surface. Very clean, flat surfaces in which the pore-grain boundaries appear in high contrast have been generated with no apparent distortion of the pore boundaries. The method is suitable to local nanometer scale 3D imaging of selected volumes in large samples.

The nanoscale resolution 3D image of the chalk pore space has been analyzed regarding the pore sizes, equilibrium fluids distribution, and capillary pressure. To process the image, methods described in Silin *et al.*, 2003, Jin, *et al.*, 2004 have been applied. The distinctive feature of these methods is that the image of the pore space is analyzed directly, bypassing pore network extraction. The methods and algorithms used in this study admit modifications to account for mixed wettability, mechanical deformations and damage of the rock and studies of double porosity media.

It has been observed that besides the two orders of the magnitude length scale difference, the chalk images have some qualitative features distinguishing them from sandstone. Most noticeable is the presence of relatively large openings, which manifest themselves as almost horizontal intervals on the drainage capillary pressure curve. There is significant local pore space heterogeneity associated with these larger openings, which makes the appropriate choice of representative imaging sample size a critical issue.

The dimensionless capillary pressure curve provides a signature representation of rock type and can be used as a criterion of success of the computer rock reconstruction. By appropriate scaling, dimensional capillary pressure curves have been generated. Both the shapes of the curves and the absolute values of the pressures are in good agreement with published laboratory data.

ACKNOWLEDGMENTS

This work has been performed at Lawrence Berkeley National Laboratory of the U.S. Department of Energy under Contract No. DE-AC03-76SF00098. The work of the second author was partially supported by ChevronTexaco through UCOil Consortium. The Ekofisk chalk sample was provided by ConocoPhillips. The authors thank D. Maloney, J. Howard and E. Spinler from ConocoPhillips for constructive discussions and E. Spinler for permission to use data from SCA-9705. The authors express their gratitude to Dr. V. Radmilovic of

LBNL for his technical assistance and advice in image acquisition using focused ion beam. Manuscript review and valuable remarks from Prof. Tad Patzek of LBNL and UC Berkeley are greatly appreciated.

REFERENCES

Barenblatt G.I., Patzek T.W., Silin D.B. “The mathematical model of nonequilibrium effects in water-oil displacement”, SPE Journal. 8(4):409-416, 2003

Blunt, M. J. “Flow in porous media - pore-network models and multiphase flow”, Current Opinion in Colloid & Interface science, 6(3): 197–207, 2001.

Coles, M.E., Hazlett, R.D., Spanne, P., Soll, W.E., Muegge, E.L., and Jones, K.W., Pore level imaging of fluid transport using synchrotron X-Ray microtomography”, SCA9628 Society of Core Analysts Annual Technical Conference, September 8-10, 1996.

Jasty, J.K., Jesion, J., and Feldkamp, L., “Microscopic imaging of porous media with X-ray computed tomography”, SPE Formation Evaluation 189-193, September 1993.

Jin,G., Patzek, T.W. , and D. B. Silin. Physics-based reconstruction of sedimentary rocks. SPE paper 83587 SPE Western Regional/ AAPG Pacific Section Joint Meeting, Long Beach, California, USA, 2003.

Jin,G., Patzek, T.W., and D. B. Silin. Reconstruction of sedimentary rock based on mechanical properties. Physical Review E, Submitted, 2004.

Jin,G., Patzek, T.W., and D. B. Silin, SPE, Direct prediction of the absolute permeability of unconsolidated and consolidated reservoir rock. SPE paper 900084. SPE Annual Technical Conference and Exhibition, Houston, Texas, 2004.

Heaney, P.J., Vicenzi, E.P., Gianuzzi, L.A., and Livi, J.T., Focused Ion Beam Milling: A Method of Site Specific Sample Extraction for Microanalysis of Earth and Planetary Materials,” *American Mineralogist*, (2001), **86**, 1094.

Kubis, A.J., G. J. Shiflet, D.N.Dunn and R.Hill, “Focused Ion Beam Tomography”, *Metalurgical and Material Transactions A*, vol. 35A, p. 1935-1943, 2004

Lindquist, W.B.” Quantitative analysis of three dimensional X-ray tomographic images”, Development of X-ray Tomography III, U. Bouse (ed), Proceedings of SPIE 4503, 103 SPIE, Bellingham, WA 2002, ftp://ams.sunusb.edu/pub/papers/2001/susb01_06.pdf

Magnani, F. S., P. C. Philippi, Z. R. Liang, and C. P. Fernandes. “Modelling two-phase equilibrium in three-dimensional porous microstructures.” *International Journal of Multiphase Flow*, 26(1): 99–123, 2000.

Mardia, K.V. and T.J.Hainsworth, “ A spatial thresholding method for image segmentation” , IEEE Trans. Patt Anal. Mach. Intell. 10(6), pp 919-927, 1988.

Meijering, E. H., W. W. J. Niessen, M. A. Viergever. Quantitative Evaluation of Convolution-Based Methods for Medical Image Interpolation, *Medical Image Analysis*, vol. 5, no. 2, June 2001, pp. 111-126

Muskat. M, Physical principles of oil production McGraw-Hill, 1949

Oh, W., and W.B. Lindquist, “Image thresholding by indicator krigging”, IEEE Trans. Patt Anal. Mach. Intell. 21, pp 590-602, 1999.

Øren, Pal-Eric, S. Bakke, and O. J. Arntzen. Extending predictive capabilities to network models. SPE Journal, (December):324–336, 1998.

Øren, Pal-Eric and Stig Bakke. Process based reconstruction of sandstones and prediction of transport properties. *Transport in Porous Media*, 46(2-3):311–343, 2002.

Orloff, J., L. Swanson, and M. Utlaut, “High Resolution Focused Ion Beams: FIB and Its Applications : The Physics of Liquid Metal Ion Sources and Ion Optics and Their Application to Focused Ion Beam Technology” J, Kluwer Academic Publishers; (November 1, 2002)

Patzek, T. W.. Verification of a complete pore network model of drainage and imbibition. SPEJ, 6(2):144–156, 2001.

Seright, R. S., Liang, J., Lindquist, W.B., and Dunsmuir, J.H., “Use of X-Ray Computed Microtomography to Understand why gels reduce relative permeability to water more than that to oil”., *Journal of Petroleum Science and Engineering* 39, (2003), pp. 217-230.

Silin, D B. and Tad Patzek. NetSimCPP: Object-Oriented Pore Network Simulator. Lawrence Berkeley National Laboratory, 2001.

Silin, D B. and T. W. Patzek. Object-oriented cluster search for an arbitrary pore network. Technical Report LBNL-51599, Lawrence Berkeley National Laboratory, Berkeley, CA, January 2003.

Silin, D B., Guodong Jin, and Tad.W. Patzek. Robust Deteremination of the Pore-space Morphology in Sedimentary Rocks. *Journal of Petroleum Technology*, May: 69–70, 2004.

Silin, D B., Patzek T. On Barenblatt's model of spontaneous countercurrent imbibition. *Transport in Porous Media*. 54(3):297-322, 2004

Spinler, E. A. and B. A. Baldwin. Capillary pressure scanning curves by direct measurement of saturations. SCA-9705, 1997 International Symposium of the Society of Core Analysts, Calgary, Alberta, Canada, 8_10 September 1997

Stampanoni, M, Borchart, G., Abella, R and P. Ruegsegger, "Bragg Magnifier: A detector for submicrometer x-ray computer tomography", *Journal of Applied Physics*, (2, no. 12, pp7630-7635, 15 December 2002

Talukdar, M.S., Ioannidis, M., Howard, J., and Torsaeter, O., "Network modeling as a tool for petrophysical measurements in chalk," *Proceedings of the 6th Nordic Symposium on Petrophysics*, (15-16 May 2001), Trondheim, Norway.

Tomutsa, L. and V. Radmilovic, Focused Ion Beam Assisted Three-dimensional Rock Imaging at Submicron Scale, SCA2003-47, 2003 International Symposium of the Society of Core Analysts, Pau, France, 21-24 September 2003.

Wildenschild, D., J.W. Hopmans, C.M.P. Vaz, M.L. Rivers, and D. Rikard, 2002. Using x-ray computed tomography in hydrology: Systems, resolutions, and limitations. *Journal of Hydrology*, 267(3-4), 285-297.

Xu, B., J. Kamath, Y. C. Yortsos, and S. H. Lee. Use of pore-network modeling to simulate laboratory corefloods in a heterogeneous carbonate sample. *SPE Journal*, 4(3): 179-186, 1999.